Phase behaviors and ordering dynamics of diblock copolymer self-assembly directed by lateral hexagonal confinement

Yuci Xu, Nan Xie, Weihua Li, Feng Qiu, and An-Chang Shi

Citation: J. Chem. Phys. **137**, 194905 (2012); doi: 10.1063/1.4765098
View online: http://dx.doi.org/10.1063/1.4765098
View Table of Contents: http://jcp.aip.org/resource/1/JCPSA6/v137/i19
Published by the American Institute of Physics.

Phase behaviors and ordering dynamics of diblock copolymer self-assembly directed by lateral hexagonal confinement

Yuci Xu,[1,a)] Nan Xie,[1,a)] Weihua Li,[1,b)] Feng Qiu,[1,2] and An-Chang Shi[3]
[1]*State Key Laboratory of Molecular Engineering of Polymers, Department of Macromolecular Science, Fudan University, Shanghai 200433, China*
[2]*Key Laboratory of Computational Physical Sciences, Ministry of Education of China, Shanghai 200433, China*
[3]*Department of Physics and Astronomy, McMaster University, Hamilton, Ontario L8S 4M1, Canada*

(Received 23 August 2012; accepted 8 October 2012; published online 21 November 2012)

The thermodynamics and kinetics of the self-assembly of cylinder-forming diblock copolymers directed by the lateral confinement of hexagons have been studied by the combination of self-consistent field theory (SCFT) calculation and time-dependent Ginzburg-Landau (TDGL) theory simulation. The SCFT calculations are used to determine the stability of candidate 2D and 3D equilibrium phases formed in small-size hexagons. Our phase diagram predicts the existence of stable phase regions with respect to the hexagonal size, which is centered around the optimal size with an extent of about a period, for the phases of perfect hexagonal cylinders. Our TDGL simulations reveal that the ordering event, in which the structure evolves toward the perfect state, occurs stochastically according to the Poisson distribution, and the ordering time grows roughly with a power-law relation of the hexagonal size. This prediction is helpful to estimate the annealing time for larger systems with the knowledge of the annealing time of a small system in experiments. © *2012 American Institute of Physics*. [http://dx.doi.org/10.1063/1.4765098]

I. INTRODUCTION

The self-assembly of block copolymers (BCPs) provides an important platform for the fabrication of ordered micropatterns which have potential applications in the manufacture of nanoscale functional materials.[1–10] In practice, the BCP self-assembly is used to extend the feature size of nanolithography into finer size for sub-30-nm patterns in nanotechnology applications,[3,8,11,12] thus decreasing the cost of present lithography techniques (e-beam or extreme ultraviolet lithography). The technique of combining the BCP self-assembly and lithography is referred as the BCP lithography, in which the BCPs are spin coated onto sparcely patterned substrates obtained by lithography and then the BCP phase separation takes place under the direction of the pattern. The shortcoming of absence of long-range order in the microstructures formed by BCP self-assembly can be overcome by the direction of the patterned substrates, and thus large-scale perfectly ordered patterns can be achieved.[13–21] The directing efficiency of this lithography technique is described by the density multiplication (DM), which can quantify the ratio of the number of self-assembled BCP domains to the number of directing substrate pattern units in a given area or volume of the sample. A larger DM means sparser substrate feature is required, thus reducing the manufacturing cost. At the same time, a larger DM reduces the directing ability of the pattern, and therefore, increases the probability for defects to be caused.[22–27] Large-scale dynamic simulations in two-dimensional (2D) space predict that the defect evolution of hexagonal cylinders on 2D hexagonally patterned surfaces follows an exponential-decay law when the DM is not larger than 16, while it becomes close to the evolution behavior on uniform substrate, i.e., multi-step power law, when DM is 36.[24] This suggests that the upper limit of DM is not larger than 25 when the surface pattern has ideal directing effect. After taking the factor of film thickness and other experimental factors into account, such as BCP polydispersity, small incommensurability between the periods of the BCP domain array and the substrate pattern, the DM in experiments should be smaller than 25. To date, the largest DM from the 2D patterned substrates realized by experiments is 9.[14] The DM can be raised to be higher by introducing 3D directing patterns, for example, patterned nanoposts on substrates.[12] Nevertheless, the DM is still very limited. It has been proposed that the principle reason for the limit is the microphase separating kinetics of BCPs often involved in the BCP self-assembling process, i.e., spinodal or near spinodal decomposition, where the microphase separation occurs rapidly and globally. Based on this mechanism, extremely high DM is just obtained via the BCP phase separation of nucleation on the patterned substrates by computer simulations.[25] However, the research of the new scheme is at the primary stage. An alternative directing method is the geometrical confinement.

The BCP self-assembly under geometrical confinements has been of great interest in both experiments and theories for decades. Geometrical confinement can be 1D (thin films),[28–36] 2D (cylindrical),[37–51] and 3D (spherical or non-spherical).[52–56] The introduction of geometrical confinements results in the formation of many novel microstructures by breaking the intrinsic symmetry in the BCP bulk

[a)] Y. Xu and N. Xie contributed equally to this work.
[b)] Author to whom correspondence should be addressed. Electronic mail: weihuali@fudan.edu.cn.

phases.[57,58] For example, a number of interesting structures, including single/double helices, toroids, stacked disks, have been observed in cylinder-forming BCPs under a cylindrical confinement by experiments,[38–40,50,51] computer simulations,[37,43–45,48] and theoretical calculations of self-consistent field theory (SCFT).[41,42,46] During the structure formation, the geometrical shape of confinement also plays an important role. A systematic study on the influence of the nanopore shape on the structure formation of cylinder-forming BCPs has been carried out using Monte Carlo (MC) simulations by Li and co-workers.[59] In ideal circular cylindrical nanopores, it is rare to observe structures of straight cylinders aligning along the pore axis as a stable phase except for the formation of a central cylinder in narrow pores.[42] When the pore shape is changed to be a regular hexagon, thus sharing the symmetry of the bulk phase, the double-layer hexagonal cylinders (seven cylinders) have been observed in a range of pore diameter (about 3-3.2 L_0, where L_0 is the cylinder-to-cylinder distance).[59] This existence of hexagonal cylinders in the hexagonally confined BCPs indicates that the hexagonal confinement has the potential to become an effective method to direct BCPs to form perfect hexagonal patterns in large scale. The results of MC simulation suggest that the phases of hexagonal cylinders compete with other 3D structures, for example, a number of helical phases.[59] However, as MC simulation is not capable to determine the relative stability between different structures, the exact stability region has not been calculated, yet. The stability region of hexagonal cylinders is a useful guide for the lithography application via the lateral hexagonal confinement. Furthermore, it is helpful to gain further understanding on the influence of the pore shape on the structure formations by comparing the phase diagram with that of the circular cylindrical confinement. Therefore, to identify the phase diagram with respect to the hexagonal size is important for both application and theory. The SCFT based on Gaussian chain model is one of the most successful theories to determine the relative stability of BCP-formed phases because it can compute accurately their free energy.[60,61] In addition, the pseudo-spectral method of SCFT is also high efficient to search new structures.[62,63] Therefore, we use the pseudo-spectral method of SCFT to explore the phase stability of structures formed in cylinder-forming diblock copolymers under the hexagonal confinement.

In general, the technique of BCP lithography involves a system size as large as microns. In very recent experiments, Xu *et al.* have designed an effective hexagonal confinement to direct the self-assembly of diblock copolymers toward perfectly ordered hexagonal cylinders in large scale.[17] The substrate patterns are fabricated by using metal-coated atomic force microscope tip to oxidize the terminal methyl group into carboxylic acid groups. The chemical contrast between the patterned and unpatterned regions acts as an effective lateral hexagonal confinement, under which perpendicular hexagonal cylinders are formed because of the slightly preferential surfaces used in the experiments. Defect-free cylinder patterns are observed in a hexagon with its longest diagonal (D), as large as 500 nm, containing 161 cylinders. According to the number of cylinders aligned along its longest diagonal, D is roughly equal to $15L_0$. For larger hexagons, such as D $\approx$ 600 nm and 1175 nm, small amount of defects are present in the patterns. When increasing the hexagonal size further, the number of defects is noticeably increased. The ordering degree of the patterns formed by the BCP self-assembly confined in such large hexagons is dependent not only on the thermodynamics, but also on the kinetics. Theoretically, Fredrickson and co-workers have examined the ordering and defect formation of cylinder-forming diblock copolymers as well as homopolymer/diblock copolymer blends under the lateral hexagonal confinement using 2D SCFT calculations.[64] Their calculations predict the commensurability window, where a well-ordered cylinder pattern is achieved, with a hexagonal size of around $D \sim 9L_0$. Their results predict that the window width in three cases of lateral surface preferences, (a) the majority attractive, (b) neutral, and (c) the minority attractive, is $\Delta D \approx 2.5R_g$, $0.5R_g$, and R_g, respectively, under the quenching condition. While under the temperature annealing condition, which is mimicked by slowly incrementing χN, the window width is increased tremendously for all three cases, especially for the latter two cases. However, the examined hexagon is obviously smaller than those in experiments because of the limit of the computational time. Furthermore, their theory is basically an equilibrium one, and a careful investigation on the ordering kinetics of the present confined system is still lacking. Therefore, it is desirable to explore the ordering kinetics of BCP self-assembly under the confinement of large hexagons which have comparable size to those in experiments. It has been well established that the cell dynamic simulation (CDS) based on the time-dependent Ginzburg-Landau (TDGL) model is an efficient kinetic method which can describe the collective kinetics of the BCP self-assembling behaviors.[65–67] Its high efficiency allows us to examine a system of size as large as microns which is the typical size examined by experiments.[23,24]

In the present work, we focus on the study of the self-assembling behaviors of AB diblock copolymers under the hexagonal confinement by using SCFT calculation as well as TDGL simulation. First, the SCFT is used to explore the phase behaviors of BCPs in narrow hexagons, and thus, to predict the stable phase region of hexagonally packed cylinders. Then, we use the TDGL simulation to examine the ordering kinetics of BCPs in large hexagons where the hexagonal phases are stable in equilibrium. The aims of the kinetic simulations are to determine the ordering time (or annealing time) for different hexagons, and to understand the ordering mechanism by analyzing the defect evolution.

II. THEORY AND MODEL

A. Self-consistent field theory

We consider an incompressible melt of AB diblock copolymers confined in a regular hexagonal pore with a side length of R, and the longest diagonal of D (D = 2R). Each polymer chain has an equal polymerization N, and the volume fraction of A is set by the ratio of $f = N_A/N$, where N_A is the polymerization of A block. Lengths in our SCFT calculations are expressed in units of the radius of gyration, R_g. Within the mean-field approximation to statistical mechanics

of the Edwards model of polymers,[61,68] the free energy functional F for n Gaussian diblock copolymer chains at a given temperature T is written as

$$\frac{F}{nk_BT} = -\ln Q + \frac{1}{V}\int_V d\mathbf{r}\{\chi_{AB}N\phi_A(\mathbf{r})\phi_B(\mathbf{r}) - w_A(\mathbf{r})\phi_A(\mathbf{r}) - w_B(\mathbf{r})\phi_B(\mathbf{r}) - \eta(\mathbf{r})[1-\phi_A(\mathbf{r})-\phi_B(\mathbf{r})] + H_{SCFT}(\mathbf{r})[\phi_A(\mathbf{r})-\phi_B(\mathbf{r})]\}, \quad (1)$$

where ϕ_A and ϕ_B are the monomer densities. The quantity Q is the partition function of a single polymer chain interacting with the mean fields w_A and w_B, which are produced by the surrounding chains, under the incompressible condition enforced by the Lagrange multiplier of $\eta(\mathbf{r})$. In the confined melt, the spatial integration is restricted to the pore volume, taken to be V. A function, $H_{SCFT}(\mathbf{r})$, is used to describe the preferential potential of the lateral walls of hexagons on the two species. Wang *et al.* have carried out a careful study on the influence of the surface potential form on the phase behaviors in confined BCP systems, and their results suggest that different forms of surface potential have rather limited influence on the formation of morphologies as well as the phase transitions.[69] A similar expression as those used in our previous work is applied,[70]

$$\frac{H_{SCFT}(\mathbf{r})}{\chi N} = V_0\{\exp[(\sigma - d(\mathbf{r}))/\lambda] - 1.0\} \quad (2)$$

when the closest distance $d(\mathbf{r})$ between the position $\mathbf{r}$ inside the hexagon and any side is smaller than $\sigma = 0.5R_g$, and otherwise, the surface potential is set to zero. The quantity $\lambda = 0.25R_g$ characterizes the steepness of the surface potential, and the positive constant $V_0 = 0.2$ indicates that the pore wall has a rather strong attraction to the majority blocks.[70] Minimization of the free energy with respect to the monomer densities and the mean fields leads to the following SCFT equations[61]

$$\begin{aligned} w_A(\mathbf{r}) &= \chi_{AB}N\phi_B(\mathbf{r}) + H_{SCFT}(\mathbf{r}) + \eta(\mathbf{r}),\\ w_B(\mathbf{r}) &= \chi_{AB}N\phi_A(\mathbf{r}) - H_{SCFT}(\mathbf{r}) + \eta(\mathbf{r}),\\ Q &= \tfrac{1}{V}\textstyle\int_V d\mathbf{r}q(\mathbf{r},s)q^\dagger(\mathbf{r},s),\\ \phi_A(\mathbf{r}) &+ \phi_B(\mathbf{r}) = 1. \end{aligned} \quad (3)$$

In the above equations, $q(\mathbf{r}, s)$ and $q^\dagger(\mathbf{r}, s)$ are end-segment distribution functions.[61] These distribution functions satisfy the modified diffusion equations

$$\frac{\partial q(\mathbf{r},s)}{\partial s} = \nabla^2 q(\mathbf{r},s) - w(\mathbf{r},s)q(\mathbf{r},s), \quad (4)$$

$$-\frac{\partial q^\dagger(\mathbf{r},s)}{\partial s} = \nabla^2 q^\dagger(\mathbf{r},s) - w(\mathbf{r},s)q^\dagger(\mathbf{r},s), \quad (5)$$

where $w(\mathbf{r}, s) = w_A(\mathbf{r})$ for $s < f$ and otherwise $w(\mathbf{r}, s) = w_B(\mathbf{r})$. The initial conditions are $q(\mathbf{r}, 0) = q^\dagger(\mathbf{r}, 1) = 1$. For numerical solutions, we employ the second-order operator-split method (or the pseudo-spectral method),[62,63] to solve the modified diffusion equations for the end-segment distribution functions.

The cross section of the pore is set in the x-y plane, and is put into a rectangular box whose size is slightly larger than the longest diameter of the pore. To regulate the calculations, the 2D morphologies with translational symmetry along the pore axis are examined in 2D calculations, and the 3D structures are examined in full 3D calculations. In 3D calculations, the pore axis is aligned along the z direction. For the pseudo-spectral method, periodic boundary conditions are imposed automatically on the simulation box. The box is discretized into a lattice of $N_x \times N_y$ in 2D, or $N_x \times N_y \times N_z$ in 3D. The lattice size in the x-y plane is chosen as 128 or 256 according to the pore size to ensure the lattice spacing is smaller than $0.1R_g$, and N_z is chosen as 64. The chain contour is divided into 200 segments. More details about the SCFT calculations for confined BCP systems can be found in our previous work.[41,42]

B. Time-dependent Ginzburg-Landau theory

The density difference, $\phi(\mathbf{r}) = \phi_A(\mathbf{r}) - \phi_B(\mathbf{r})$, is chosen as the order parameter to describe the phase separation and the pattern formation of the diblock copolymer. The model free energy can be written as a functional of ϕ which consists of three parts: short-range, long-range, and the contribution term from the surface field, $H_{TDGL}(\mathbf{r})$:[71]

$$F[\phi] = F_S[\phi] + F_L[\phi] + \int d\mathbf{r}H_{TDGL}(\mathbf{r})\phi(\mathbf{r}). \quad (6)$$

The short-range part F_S is the usual Ginzburg-Landau free energy and is given by

$$F_S[\phi] = \int d\mathbf{r}\left\{\frac{C}{2}[\nabla\phi(\mathbf{r})]^2 + W(\phi)\right\}, \quad (7)$$

where C is a positive constant, $W(\phi)$ is the local interaction contribution, and it can be specified by its derivative:

$$\frac{dW(\phi)}{d\phi} = -A_0\tanh(\phi) + \phi, \quad (8)$$

with a constant of $A_0 > 1$ for the phase separation between A and B. The long-range contribution is originally proposed by Ohta and Kawasaki to alter the phase separation from macroscopic in A/B blends to be microscopic in AB diblock copolymers,[71] which is expressed as

$$F_L(\phi) = \frac{\alpha}{2}\int d\mathbf{r}\int d\mathbf{r}'G(\mathbf{r}-\mathbf{r}')\delta\phi(\mathbf{r})\delta\phi(\mathbf{r}'), \quad (9)$$

where $\delta\phi(\mathbf{r}) = \phi(\mathbf{r}) - \bar{\phi}$, and $\bar{\phi} = 2f - 1$ is the average value of $\phi(\mathbf{r})$ over the whole space. In the above expression, $G(\mathbf{r} - \mathbf{r}')$ is the Green function, which can be conveniently specified by

$$-\nabla^2 G(\mathbf{r}-\mathbf{r}') = \delta(\mathbf{r}-\mathbf{r}'). \quad (10)$$

The positive coefficient α in expression (9) is proportional to $1/N^2f(1-f)$, and is inherent to the block copolymer.[65,72] Similar as the scheme in the SCFT calculations, the $H_{TDGL}(\mathbf{r})$ in the last term of Eq. (6) acts as the preferential potential of the lateral walls on the two species. An alternative form of the potential is applied,

$$H_{TDGL}(\mathbf{r}) = -\frac{1}{2}U_0\{\tanh[(\sigma - d(\mathbf{r}))/\epsilon] + \mathbf{1}\}, \quad (11)$$

when the shortest distance of the position $\mathbf{r}$ to any side of the hexagonal pore, $d(\mathbf{r}) < 2\sigma$. The quantities U_0, σ, and ϵ have

similar physical meaning as those in the expression (2), but have different values because of the difference of parameters between the SCFT model and the TDGL model. Though the different forms of the surface potential are used in the SCFT and TDGL models, both of them are short-range surface potential. Therefore, the potential form has rare influence on the simulation results, especially for the case of $D \gg \sigma$.

With the above free-energy functional, the dynamics of the density evolution can be described by the Cahn-Hilliard model (Model B):[65–67]

$$\frac{\partial \phi}{\partial t} = M\nabla^2 \frac{\delta F[\phi]}{\delta \phi} + \zeta(\mathbf{r}, t), \tag{12}$$

where M is a phenomenological mobility coefficient, set to $M = 1$, and $\zeta(\mathbf{r}, t)$ is a random noise term, with zero average and a second moment of $\langle \zeta(\mathbf{r}, t)\zeta(\mathbf{r}', t')\rangle = -\zeta_0 M\nabla^2\delta(\mathbf{r} - \mathbf{r}')\delta(t - t')$, here ζ_0 is the noise strength.

We choose these parameters $f = 0.39$, $A_0 = 1.30$, $\alpha = 0.02$, and $\zeta_0 = 0.04$ to obtain the typical hexagonal cylinder phase in bulk, and choose these parameters of the surface potential as $U_0 = 0.02$, $\sigma = 0.15L_0$, and $\epsilon = 0.5L_0$ (L_0 is the cylinder-to-cylinder distance in the bulk cylinder phase). In the experiments of BCP lithography by Xu *et al.*,[17] the hexagonal confinement is realized in a thin film with the thickness slightly less than L_0. Although a periodic array of hexagons are examined simultaneously, they are independent on each other. Therefore, only one hexagon is simulated in each run which is carried out in 3D space. The top and bottom surfaces are assumed to be neutral to allow the formation of perpendicular cylinders in the thin film, and the lateral walls are attractive to the majority block. In practice, the reflective boundary conditions are utilized on the two surfaces. The CDS method, where the forward Euler algorithm is applied for the time integration and the explicit finite differential scheme is applied for the space, has been proven to be efficient to solve the TDGL equations.[24] When the lattice spacing in the CDS simulations is fixed as $\Delta x = \Delta y = \Delta z \equiv \Delta = 0.5$, the time step Δt is chosen as 0.1 to ensure the evolving stability of the dynamic equations. L_0 is determined as about 15.92Δ by the simulation of bulk system. In order to reduce the simulation time of large hexagons with comparable sizes to those in experiments,[17] we fix our film thickness to a small value, $L_z \approx 0.4L_0$, which means that the height of the hexagonal pore is small. In this case, we can focus on the structure evolution in the x-y planes of the cross section, and at the same time, we also include the influence of the presence of the top-bottom surfaces on the ordering process by the simulation of 3D thin films.

III. RESULTS AND DISCUSSION

A. SCFT calculations of the phase behaviors

The consistent symmetry between the hexagonal confinement and the hexagonal cylinder phase suggests that hexagonally arranged cylinders cut by the pore wall should be the most preferred morphology when the pore size is commensurate with the bulk period. That MC simulations observed seven hexagonally arranged cylinders in the hexagon with an appropriate size provides a simple proof.[59] However, the stability regions of hexagonal phases are not determined by MC simulations. Furthermore, the phase behaviors in the present system are rather similar as those in the circular cylindrical confinement. A more careful study based on the SCFT calculations is required to identify the phase diagram and to reveal the difference between the phase diagrams of the hexagonal and circular confinements. For a typical cylinder-forming diblock copolymer, with fixed parameters of $\chi N = 20$ and $f = 0.26$, first we explore the possible equilibrium solutions of SCFT equations by a large number of random initial conditions for each hexagon in the 2D space. By comparing the free energy of these 2D phases, their relative stability as well as their stable phase sequence as a function of the hexagonal size is identified. The stable 2D phases and their phase sequence are presented in Figures 1(a) and 1(b), respectively,

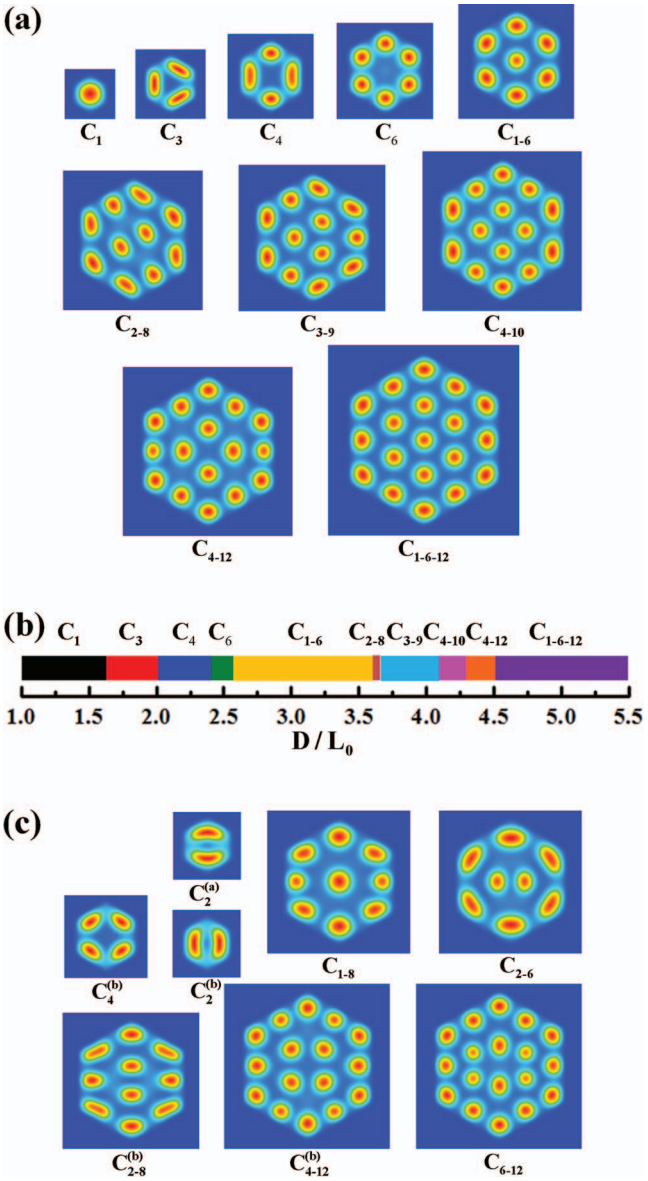

FIG. 1. (a) Density plots of stable morphologies observed in the cylinder-forming diblock copolymer melts, with fixed $f = 0.26$ and $\chi N = 20$, under the confinement of two-dimensional hexagons with varying diagonal size of D, in units of the bulk cylinder-to-cylinder distance of L_0; (b) stable phase sequence of morphologies as a function of D/L_0; (c) density plots of observed metastable 2D morphologies.

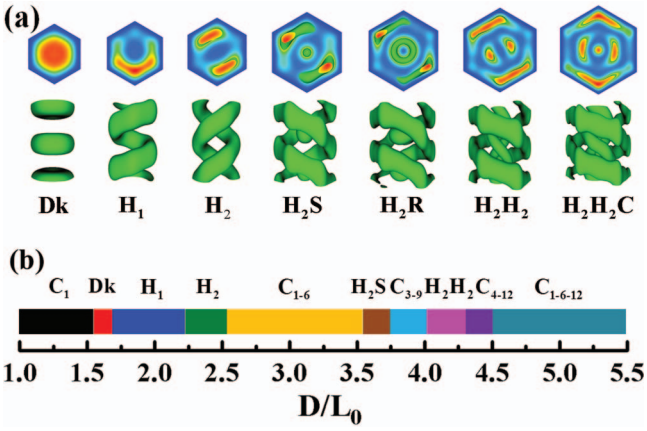

FIG. 2. (a) Isosurface density plots and the density profiles of cross section of three-dimensional morphologies. The major component inside the green isosurface is A block indicated by red-color region in the cross section profiles. (b) Stable phase sequence as a function of D/L_0 identified by considering both 2D and 3D phases.

and the observed metastable phases are shown in Figure 1(c). With the narrowest phase region of C_{2-8}, we have checked the influence of the grid lattice on the phase boundary by using a doubled grid lattice, 256 × 256. Our results suggest that the shift of phase boundary induced by the finer grid spacing is smaller than the grid spacing itself. This suggests that our calculations can give rather reliable predictions on the stable phase regions. The imposed symmetry by the hexagonal boundary makes the 2D phase sequence, $C_1 \rightarrow C_3 \rightarrow C_4 \rightarrow C_6 \rightarrow C_{1-6} \rightarrow C_{2-8} \rightarrow C_{3-9} \rightarrow C_{4-10} \rightarrow C_{4-12} \rightarrow C_{1-6-12}$, different from that in the circular confinement, $C_1 \rightarrow C_3 \rightarrow C_4 \rightarrow C_5 \rightarrow C_{1-6} \rightarrow C_{1-7} \rightarrow C_{1-8} \rightarrow C_{3-9} \rightarrow C_{4-10} \rightarrow C_{4-11} \rightarrow C_{5-11} \rightarrow C_{1-6-12}$.[41] Those phases with noticeable different symmetry from the hexagon, such as C_5, C_{1-7}, C_{4-11}, and C_{5-11} appearing in the circular confinement, are excluded by the hexagonal confinement. In addition, the stability region of the hexagonal type of phases, C_{1-6} and C_{1-6-12}, are expanded because of their consistent symmetry with the hexagonal confinement.

There are a number of intermediate structures between C_{1-6} and C_{1-6-12}, in which the domain arrangement becomes more frustrated because of the mismatch of size and symmetry. In these phase regions, the polymer chains tend to release their stretching energy through the third direction, and thus to form three-dimensional structures. All 3D structures found in full 3D SCFT calculations, including stacked disks (Dk), single helix (H_1), double helices (H_1), double helices plus spheres (H_2S), double helices plus rings (H_2R), double-double helices (H_2H_2), and double-double helices plus the central cylinder (H_2H_2C), are shown in Figure 2(a), and the new stable phase sequence, which is reconstructed by comparing the free energy of both 2D and 3D phases, is given in Figure 2(b). The free-energy comparisons of the phase diagram are presented in Figure 3. For the reason of clarity, we divide the plot of the considered region into four pieces. After including 3D phases, the stable phase sequence becomes $C_1 \rightarrow Dk \rightarrow H_1 \rightarrow H_2 \rightarrow C_{1-6} \rightarrow H_2S \rightarrow C_{3-9} \rightarrow H_2H_2 \rightarrow C_{4-12} \rightarrow C_{1-6-12}$, where most of intermediate

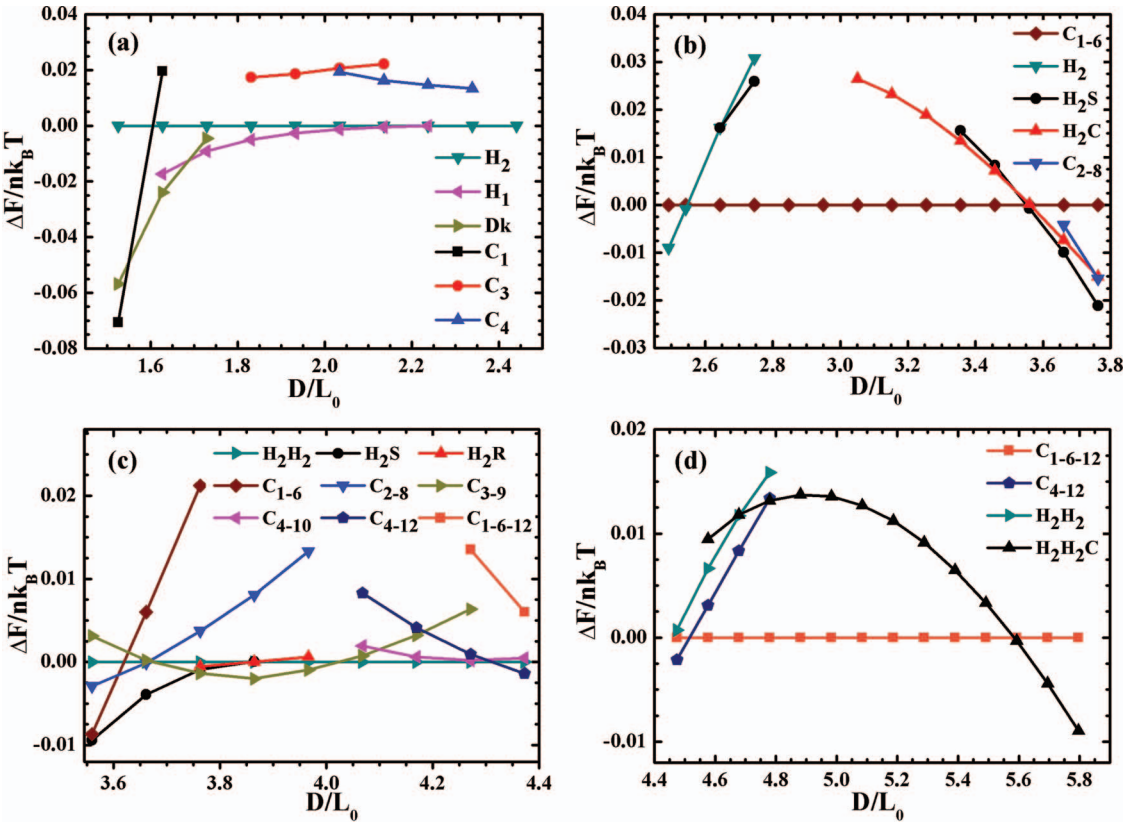

FIG. 3. Free-energy comparisons between all candidate 2D and 3D morphologies for hexagons with the diagonal size between L_0 and $6L_0$. For the reason of clarity, the free energy relative to that of a selected reference phase is plotted, and the plot is divided into four pieces along the size.

2D phases are replaced by 3D phases except for C_{3-9} and C_{4-12}. Obviously, the phase regions of the two intermediate 2D phases are narrower than those of the hexagonal 2D phases like C_{1-6} and C_{1-6-12}, which are $D/L_0 \approx 2.54$–3.55 and $D/L_0 \approx 4.51$–5.51, respectively. In the phase sequence of the circular cylindrical confinement,[42] no any 2D phase (straight-cylinder phase) is observed as a stable phase. According to the phase diagram of narrow hexagons, we can predict the existence of the stable phase region of multi-layer hexagonal cylinders, with a width of around L_0, for large hexagons. This prediction suggests that it is feasible to use the lateral hexagonal confinement to direct large-scale perfectly ordered hexagonal patterns from the aspect of thermodynamics. However, as the relaxation time of polymer systems is long, the ordering time (or the annealing time), which is required by the hexagonal pattern to reach its perfect state, is another dominant factor. If the ordering time is reasonable for experimental observation, the perfect pattern is realizable in practice. Otherwise, if the ordering time is as long as tens of days, it is too difficult or costly to obtain the perfect pattern.

B. TDGL simulations of the ordering kinetics

The phase diagram in Figure 2(b) predicts that the hexagonal-cylinder phase region is centered around the optimal diagonal size of D with D/L_0 being the odd number, and has a width of approximately a period of L_0. L_0 is estimated as 15.92Δ by the Fourier transformation of the density profile in bulk. First, we simulate the ordering process of structures in the hexagon of $D \approx 15L_0$, which corresponds to the diagonal size of about 500 nm for the PS-b-PEO of an overall molecular weight of $M_n = 26.5\ \mathrm{kg\,mol^{-1}}$ in the experiments by Xu *et al.*[17] Figure 4 gives a number of typical density snapshots at $t = 5 \times 10^4 \Delta t$ (a), $t = 10^5 \Delta t$ (b), and $t = 2 \times 10^5 \Delta t$ (c) during the structure evolution. Here the time unit is chosen to be the time step of $\Delta t = 0.1$, unless otherwise specified. In fact, the time unit is re-normalized by Δ^2/M. The time unit corresponds to a longer time for smaller mobility of higher molecular weight. At the initial stage of $t = 5 \times 10^4$, the phase separation just starts, and the cylinder domains are not well formed. After another $t = 5 \times 10^4$, the phase separation has been almost done. Because there are a number of defects, formed by the cylinders surrounded by five or seven neighbors, the remaining task of the system is to modulate the arrangement of these cylinders to annihilate the defects in the following time. When $t = 2 \times 10^5$, all cylinders are arranged perfectly on the hexagonal lattice. It indicates that the ordering process of the whole structure is done, and accordingly the ordering time can be recorded. To record precisely the ordering time, t_p, we have to examine the ordering degree of structures by a small time interval, and here we choose it to be $10^4 \Delta t$.

For a stable perfect morphology in thermodynamics, the ordering time toward its perfect state is the most critical quantity from the aspect of kinetics. In our simulations, we find that the ordering process is a typical stochastic event for a given system with fixed hexagonal size. To explore the distribution of the ordering time, we run 100 sample simulations, starting from random disordered configurations, within a maximum time step of 10^6 for a given hexagon. Figure 5 presents the distributions of the ordering time for (a) $D/L_0 = 13$ and (b) $D/L_0 = 15$, respectively. It is known that the Poisson distribution is a discrete probability distribution that expresses the probability of a given number of events

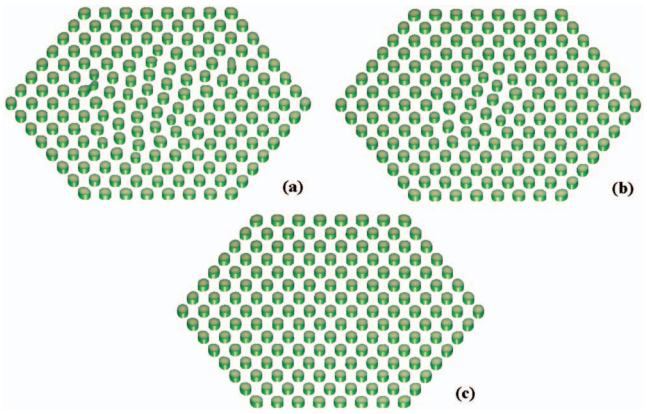

FIG. 4. Typical snapshots of density isosurfaces at $t = 5 \times 10^4 \Delta t$ (a), $t = 10^5 \Delta t$ (b), and $t = 2 \times 10^5 \Delta t$, respectively, for the diagonal size of the hexagon, $D/L_0 = 15$.

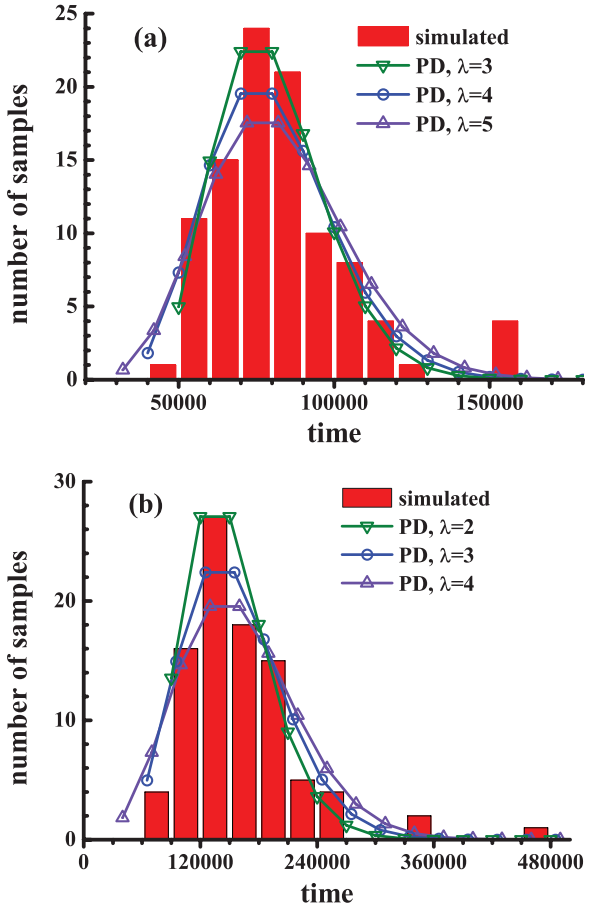

FIG. 5. Histogram plots of the distributions of the ordering time for the diagonal size of $D/L_0 = 13$ (a) and $D/L_0 = 15$ (b), respectively. The Poisson distribution is used to fit the results. (a) The time interval is chosen as $\delta t = 10^4$ time steps, and the Poisson distribution curves of three parameters of $\lambda = 3$, 4, and 5, are plotted; (b) The time interval is chosen as $\delta t = 3 \times 10^4$, and $\lambda = 2$, 3, and 4, respectively.

occurring in a fixed interval of time and/or space if these events occur with a known average rate and independently of the time since the last event. Here the events that a given system reaches its perfect state in the ordering time roughly satisfies the Poisson distribution. To fit the distribution of the ordering time with the Poisson distribution, first we must choose an appropriate time interval, δt. Then the ordering time, t_p, can be marked by a integer number, k, when $k\delta t < t_p < (k + 1)\delta t$ ($k = 0, 1, 2, \ldots$). The probability that the ordering event for a perfect pattern occurs at the time interval of k is given by the Poisson distribution as $f(k; \lambda) = \lambda^k e^{-\lambda}/k!$, where λ is equal to the expected value of k. In Figure 5(a), $D/L_0 = 13$, we choose $\delta t = 10^4$. Three fitted curves of Poisson distribution are plotted with $\lambda = 3$, 4, and 5, and with time shifts toward the time increasing direction of $t_0 = 4.5 \times 10^4$, 3.5×10^4, and 2.7×10^4, respectively. The time shift can be accounted for by the initial stage of microphase separation, in which the cylinder domains are not well formed. In other words, the whole ordering process can be divided into two stages: the phase separating stage, t_0, and the regulating stage of the domain arrangement, t_r. Thus, the ordering time is composed of the two times, i.e., $t_p = t_0 + t_r$. In the Poisson distribution, t_r corresponds to the expectation of λ. Though the three fittings give different groups of t_0 and t_r, their sums of t_p, 7.5×10^4, 7.5×10^4, and 7.7×10^4 ($\lambda = 3$, 4, 5), are very close. In Figure 5(b) of $D/L_0 = 15$, the time interval is chosen as $\delta t = 3 \times 10^4$. The ordering time is determined by $t_p = 8.5 \times 10^4 + 2\delta t = 14.5 \times 10^4$, $6 \times 10^4 + 3\delta t = 15 \times 10^4$, and $3.5 \times 10^4 + 4\delta t = 15.5 \times 10^4$, for $\lambda = 2$, 3, and 4, respectively. Though the diagonal size is increased only 15% from $13L_0$ to $15L_0$, the required ordering time becomes almost twice.

The predicted ordering time is useful to measure the realizability of a perfectly ordered pattern under the direction of a given hexagon. To fit the ordering-time distribution of a given hexagon into the Poisson distribution is an effective method to determine the ordering time. However, it is very time-consuming as it requires a large number of running samples. We use a rougher but quicker method as a substitute to do this measurement, i.e., simple sample average. For each given hexagon, we run eight independent TDGL simulations to average the ordering time, which is given in Figure 6.

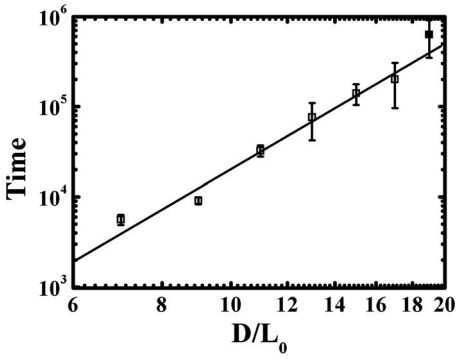

FIG. 6. Ordering time as a function of the diagonal size of hexagons, plotted in a double-logarithm plot. The solid line is obtained by a linear fitting. Note that, the filled symbol for $D = 19L_0$ indicates that the ordering time is beyond 10^6 time steps in one or more runs of our simulated eight samples.

Though the statistical error is big because of the small number of samples, it can give a good qualitative prediction. For example, the ordering time estimated with this method is $t_p = (7.6 \pm 3.4) \times 10^4$ and $(14.1 \pm 3.6) \times 10^4$, for $D/L_0 = 13$ and $D/L_0 = 15$, respectively, which are in good agreement with those measured by the Poisson-distribution fitting. The double-logarithm plot of the ordering time in Figure 6, t_p, as a function of D/L_0, shows a good linear relation. This indicates that the ordering time increases roughly according to a power-law relation, $t_p \sim (D/L_0)^{1/\nu}$, where $\nu \approx 0.22$. The underlined evolution mechanism of structures described by the power-law relation in the hexagonal confinement is consistent with that in bulk system. Usually, the time evolution of structures in bulk is measured by the evolution of the correlation length, ξ. It has been shown that the correlation length ξ grows as time according to a similar power law, $\xi \sim t^{\nu}$, where the coefficient of ν is about 1/5 or 1/4 in bulk.[73,74] In the present BCP systems under the hexagonal confinement, the perfectly ordered structure is achieved as soon as the correlation length reaches the size of the hexagon. In other words, the presence of the lateral hexagonal confinement cuts off the infinite correlation length for perfect order in bulk into a finite length, which is comparable or smaller than the hexagonal size. The simple analysis can provide a rough relation between the ordering time and the hexagonal size, i.e., $t_p \sim (D/L_0)^{1/\nu}$, which is in agreement with the prediction of our simulations. This relation is helpful for us to estimate the required ordering time for a larger system toward perfect order with the known ordering time of a small system. The diagonal sizes of hexagons in Fig. 4 of Ref. 17 are about (a) $D/L_0 \approx 15$, (b) $D/L_0 \approx 17$, (c) $D/L_0 \approx 31$, (d) $D/L_0 \approx 35$, and (e) $D/L_0 \approx 45$, respectively. The perfect hexagonal pattern is observed in the hexagon of (a), and only one defect appears in the hexagon of (b). Accordingly this indicates that the annealing time of 18 h used in the experiments is long enough for the system of (a), and it is close to the critical ordering time required by the system of (b), i.e., $t_p^{(b)} \approx 18$ h. Then we can estimate the required annealing time for the other large systems of (c), (d), and (e) using the power-law relation of $t_p \sim (D/L_0)^{1/\nu}$, which is $t_p^{(c)} \approx 276$ h, $t_p^{(d)} \approx 480$ h, and $t_p^{(e)} \approx 1503$ h, respectively. Obviously, all required annealing times by the three large systems are much longer than the real time of 18 h used in experiments. When the real annealing time is shorter than the required one, some defects are survived after the structure evolution. For a fixed annealing time, more and more defects are observed as the hexagonal size increases because the required ordering time grows fast. As soon as the required ordering time in a large hexagon becomes too long for experiments, to obtain a prefect pattern in such large system becomes impractical. For example, in the hexagon of $D/L_0 \approx 45$, the required ordering time has become as long as a couple of months. Even though we can spend such long time to anneal the sample, to keep the stable annealing conditions for such long time is also extremely challenging. Therefore, the estimation of the required ordering time for a large system can help one to set the annealing time, or to predict the possibility of achieving a perfect pattern in a large system within a reasonable annealing time. The ordering time in Figure 6 is determined for the hexagons with the almost optimal diagonal

size for the formation of perfectly ordered hexagonal cylinders, which is the odd number multiple of L_0. When the diagonal size deviates from the optimal value, it tends to cause more defects in the initial stage. Usually, it takes a longer time to eliminate more defects. In addition, the average global stress induced by the size deviation slows down the annihilating process of defects, too. For example, when $D/L_0 = 15$ is increased to $D/L_0 \approx 15.24$, the ordering time is increased from $(14.1 \pm 3.6) \times 10^4$ to $(24.12 \pm 9.54) \times 10^4$. Therefore, when there is a small deviation of the hexagonal size from the optimal value, it is necessary to prolong the corresponding annealing time in experiments.

The ordering process of the structures is helpful for one to understand the ordering mechanism. The evolution of the defect concentration is an effective quantity to measure the structure evolution, especially in a large-scale system.[24] However, the size of the present system is not as large as general bulk systems, and furthermore, the number of defects is small because of the direction of the hexagonal walls. These limiting factors can induce large statistical error in the computation of defect concentrations. Therefore, we need to look for an alternative quantity. Bosse *et al.* have proposed an alternative quantity, the space fluctuation of the bonds connecting two neighbor cylinders, which can be defined as[64]

$$\theta = \frac{1}{\bar{L}}\sqrt{\frac{\sum_{n=1}^{N_{\rm bd}}(L_n - \bar{L})^2}{N_{\rm bd} - 1}}, \tag{13}$$

where L_n is the length of bond n (all bonds are labeled by a series of integers, $n = 1, 2, \ldots$), $N_{\rm bd}$ is the total number of bonds, and $\bar{L} = \sum_{n=1}^{N_{\rm bd}} L_n / N_{\rm bd}$ is the average bond length in a given system. During the evolution, θ usually decreases to be close to zero as the structure evolves toward the perfect state, and $N_{\rm bd}$ also evolves until it reaches the final value, $(9\,m^2–12\,m + 3)/4$ (and $(3\,m^2 + 1)/4$ is the corresponding domain number), where m is the number of domains aligned on the diagonal of hexagon. Otherwise, there are fivefold or sevenfold defects, and thus the structure is not perfectly ordered. In addition, the value of θ can gives the ordering degree in some sense. In Figure 7(a), we plot the time evolution of θ for a rather large system with $D/L_0 = 21$, which corresponds to the experimental size of about 700 nm in Ref. 17.

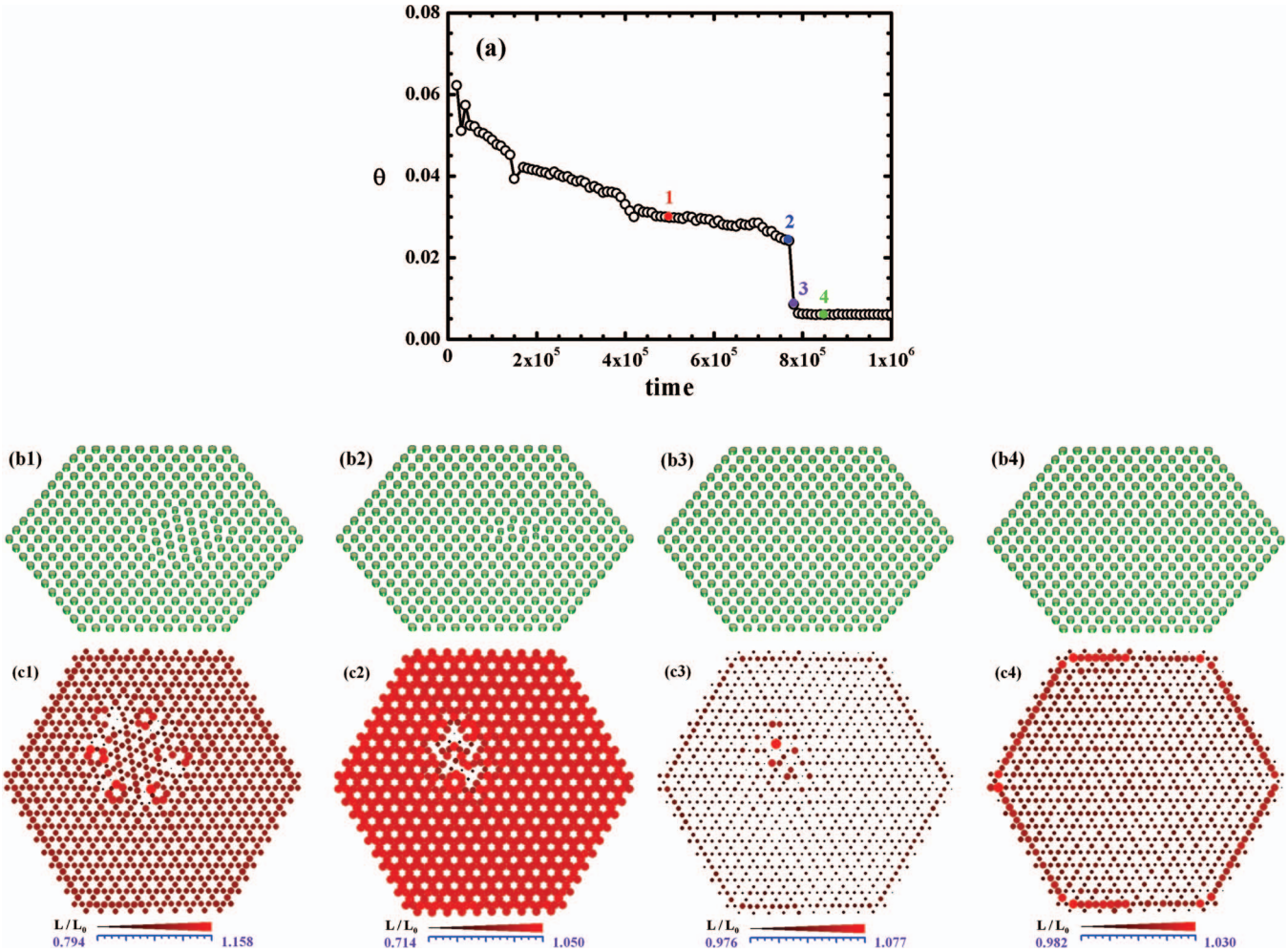

FIG. 7. (a) The time evolution of the space fluctuation of bonds, θ, for $D/L_0 = 21$. (b) Four typical snapshots of the structures are shown for $t = 50 \times 10^4$, $t = 77 \times 10^4$, $t = 78 \times 10^4$, and $t = 85 \times 10^4$, respectively (indicated by color circles and numbers 1, 2, 3, and 4) (a link to the corresponding movie of the structure evolution is provided at the end of this figure caption). (c) The corresponding distributions of bonds with respect to their positions are presented for the above four times. The bond length is indicated by both the filled circle size and the color spectrum. However, for the reason of clarity, different length ranges are used in the four plots: $L/L_0 \approx 0.794$–1.158 (c1), 0.714–1.050 (c2), 0.976–1.077 (c3), and 0.982–1.030 (c4), respectively (enhanced online) [URL: http://dx.doi.org/10.1063/1.4765098.1].

After the initial phase separating stage, θ decreases consistently and slowly from about 0.062 to 0.025 as time until the time 2 which is labeled in Figure 7(a). After the time 2, the value of θ suddenly drops to a very low value of about 0.006 within only thousands steps. To watch the structure evolution directly, the density profiles of the structures, as well as the distributions of bond length on positions, have been plotted in Figures 7(b) and 7(c) for the times, (1) $t = 50 \times 10^4$, (2) $t = 77 \times 10^4$, (3) $t = 78 \times 10^4$, and $t = 85 \times 10^4$, respectively (the corresponding movie is linked to the caption of Figure 7). The distribution of bond length is indicated by both the circle size and the color spectrum. To enlarge the length difference between bonds, different ranges of bond length are used in the four plots: (c1) $L/L_0 \approx 0.794$–1.158, (c2) 0.714–1.050, (c3) 0.976–1.077, and 0.982–1.030 (c4).The bond-length distributions obviously show that the large nonuniformity appears near the locations of defects.

In Figure 7(c1), it is seen that the defects cluster forms a boundary to separate the central domain grain and the surrounding domains as they have mismatched orientations. The cluster of defects including pairs of fivefold and sevenfold defects is difficult to be annihilated.[73,74] In this sample, the defect cluster survives until $t = 78 \times 10^4$. During the long surviving period, the system slowly regulates the domain positions around these defects to eliminate them one by one, and thus to reduce the cluster size, and finally annihilates all defects. In Figure 7(c2) of $t = 77 \times 10^4$, though the bond/domain number indicates that all defects have been eliminated, there is still noticeable nonuniformity of bond length because the system does not get time to release the stress yet when the defects are just removed. However, the further ordering process is quick because most of domain positions need to regulated slightly as soon as no any domain is added or removed. Further improvement of the bond-length distribution has been achieved in Figure 7(c3) after additional ten thousands time steps, and a nearly stable distribution for the perfectly ordered pattern is obtained, immediately. Figure 7(a) suggests that the value of θ does not go to zero, but a stable tiny value. The reason can be found in Figure 7(c4) where the domains on the first layer near walls have smaller connecting distance between each other, and those on the second layer have larger bond length. The short-distance fluctuation of bond length is induced by the surface interaction of the walls. In a summary, the size of the central grain, which is delimited by the cluster of pairs of fivefold and sevenfold defects, determines significantly the ordering time of the hexagonal system.

IV. CONCLUSIONS

The self-assembling thermodynamics and kinetics of cylinder-forming diblock copolymers under the confinement of hexagons have been systematically investigated using the SCFT calculations and the TDGL simulations, respectively. For small-size hexagons, a large number of 2D and 3D equilibrium structures are explored, and the phase diagram for stable phases with respect to the diagonal size of hexagon, is identified. The phase diagram suggests that there are a number of phases of straight cylinders, including C_{1-6}, C_{3-9}, C_{4-12}, and C_{1-6-12}, which do not appear as stable phase in the phase diagram of the diblock copolymers confined in circular nanopores. In addition, the phase regions of C_{1-6} and C_{1-6-12} are centered around the optimal size (odd number multiple of L_0) and have a extent of a period. This feature can predict that there should exist similar stable phase regions of hexagonal cylinder morphologies in large hexagons. Thus, the hexagonal confinement can be an effective external condition to direct the self-assembly of cylinder-forming diblock copolymers toward large-scale perfectly ordered patterns from the aspect of thermodynamics.

Then the ordering dynamics of cylinders, self-assembled by the diblock copolymer confined in large hexagons, is studied by the TDGL simulations. One of the most important quantities for the structure evolution is the required ordering time in which the structure evolves to reach its perfect state. First, we constructed the ordering-time distributions of structures with a large number of running samples for two given hexagons of $D/L_0 = 13$ and $D/L_0 = 15$, respectively. It is revealed that both distributions roughly satisfy the Poisson distribution. This suggests that the ordering event, that the system evolves toward the perfect state, occurs stochastically in the time interval of $[k\delta t, (k + 1)\delta t]$, according to the Poisson distribution of $f(k; \lambda)$, where $\lambda\delta t + t_0$ gives the expected ordering time together with the domain forming time of t_0. Then, we choose an alternative method of simply averaging on eight independent samples, which is rougher but quicker, to estimate the ordering time for various hexagons. Our result indicates that the ordering time is a power-law function with respect to the hexagonal size, and the power-law coefficient is as large as 4.5. This suggests that the required ordering time grows quickly as the hexagonal size increases, and thus reaching the time limit of experimental observation. For example, in the hexagon with a diagonal size of 1500 nm in the experiments by Xu *et al.*,[17] our result predicts that the required ordering time is as long as a couple of months which is rather impractical for experiments. On the other hand, this prediction is helpful for one to estimate the reasonable annealing time for larger systems with the known annealing time of a small system.

ACKNOWLEDGMENTS

This work was supported by the National Natural Science Foundation of China (NNSFC) (Grants Nos. 20974026, 21174031, and 20990231); the National High Technology Research and Development Program of China (863 Grant No. 2008AA032101); and the Natural Science and Engineering Research Council (NSERC) of Canada.

[1] ITRS International Technology Roadmap for Semiconductors. 2010 ed. Lithography. (http://www.itrs.net/Links/2010ITRS/Home2010.html).
[2] G. M. Whitesides and B. Grzybowski, Science **295**, 2418 (2002).
[3] M. Park, C. Harrison, P. M. Chaikin, R. A. Register, and D. H. Adamson, Science **276**, 1401 (1997).
[4] S. O. Kim, H. H. Solak, M. P. Stoykovich, N. J. Ferrier, J. J. de Pablo, and P. F. Nealey, Nature (London) **424**, 411 (2003).
[5] K. W. Guarini, C. T. Black, Y. Zhang, I. V. Babich, E. M. Sikorski, and L. M. Gignac, 2003 IEEE International Electron Devices Meeting, Technical Digest, Washington, DC, p. 541.

[6]M. P. Stoykovich, M. Müller, S. O. Kim, H. H. Solak, E. W. Edwards, J. J. de Pablo, and P. F. Nealey, Science **308**, 1442 (2005).
[7]M. P. Stoykovich and P. F. Nealey, Mater. Today **9**, 20 (2006).
[8]R. A. Segalman, H. Yokoyama, and E. J. Kramer, Adv. Mater. **13**, 1152 (2001).
[9]C. J. Hawker and T. P. Russell, MRS Bull. **30**, 952 (2005).
[10]I. W. Hamley, Nanotechnology **14**, R39 (2003).
[11]L. W. Chang, T. L. Lee, C. H. Wann, C. Y. Chang, and H.-S. P. Wong, 2009 IEEE International Electron Devices Meeting, p. 821.
[12]I. Bita, J. Yang, Y. S. Jung, C. A. Ross, E. L. Thomas, and K. K. Berggren, Science **321**, 939 (2008).
[13]Y. S. Jung, J. B. Chang, E. Verploegen, K. K. Berggren, and C. A. Ross, Nano Lett. **10**, 1000 (2010).
[14]Y. Tada, S. Akasaka, H. Yoshida, R. Ruiz, E. Dobisz, and H. Hasegawa, Polymer **50**, 4250 (2009).
[15]J. Y. Cheng, C. T. Rettner, D. P. Sanders, H. C. Kim, and W. D. Hinsberg, Adv. Mater. **20**, 3155 (2008).
[16]R. Ruiz, H. Kang, F. A. Detcheverry, E. Dobisz, D. S. Kercher, T. R. Albrecht, J. J. de Pablo, and P. F. Nealey, Science **321**, 936 (2008).
[17]J. Xu, S. Park, S. L. Wang, T. P. Russell, B. M. Ocko, and A. Checco, Adv. Mater. **22**, 2268 (2010).
[18]J. Chiota, J. Shearer, M. Wei, C. Barry, and J. Mead, Small **5**, 2788 (2009).
[19]K. W. Yang, Y. S. Jung, J. B. Chang, R. A. Mickiewicz, A. Alexander-Katz, C. A. Ross, and K. K. Berggren, Nat. Nanotechnol. **5**, 256 (2010).
[20]J. Y. Cheng, M. M. Anne, and R. A. Ross, Nature Mater. **3**, 823 (2004).
[21]D. Sundrani, S. B. Darling, and S. J. Sibener, Nano Lett. **4**, 273 (2004).
[22]F. A. Detcheverry, P. F. Nealey, and J. J. de Pablo, Macromolecules **43**, 6495 (2010).
[23]W. H. Li, N. Xie, F. Qiu, Y. L. Yang, and A. C. Shi, J. Chem. Phys. **134**, 144901 (2011).
[24]W. H. Li, F. Qiu, Y. L. Yang, and A. C. Shi, Macromolecules **43**, 1644 (2010).
[25]N. Xie, W. H. Li, F. Qiu, and A. C. Shi, "The self-assembling nucleation of block copolymer/homopolymer blends in bulk and on patterned substrates," Soft Matter (published online).
[26]Y. Tada, S. Akasaka, H. Yoshida, H. Hasegawa, E. Dobisz, D. Kercher, and M. Takenaka, Macromolecules **41**, 9267 (2008).
[27]Q. Y. Tang and Y. Q. Ma, Soft Matter **6**, 4460 (2010).
[28]M. W. Matsen, J. Chem. Phys. **106**, 7781 (1997).
[29]Q. Wang, Q. Yan, P. F. Nealey, and J. J. de Pablo, J. Chem. Phys. **112**, 450 (2000).
[30]A. Knoll, A. Horvat, K. S. Lyakhova, G. Krausch, G. J. A. Sevink, A. V. Zvelindovsky, and R. Magerle, Phys. Rev. Lett. **89**, 035501 (2002).
[31]J. Feng and E. Ruckenstein, Polymer **43**, 5775 (2002).
[32]H. Tan, D. Yan, and A. C. Shi, Macromolecules **37**, 9646 (2004).
[33]Y. Yin, P. Sun, T. Chen, B. Li, Q. Jin, D. Ding, and A. C. Shi, Chem. Phys. Chem. **5**, 540 (2004).
[34]Y. Z. Yang, F. Qiu, H. D. Zhang, and Y. L. Yang, Polymer **47**, 2205 (2006).
[35]G. E. Stein, E. W. Cochran, K. Katsov, G. H. Fredrickson, E. J. Kramer, X. Li, and J. Wang, Phys. Rev. Lett. **98**, 158302 (2007).
[36]S. Sakurai, H. Bando, H. Yoshida, R. Fukuoda, M. Mouri, K. Yamamoto, and S. Okamoto, Macromolecules **42**, 2115 (2009).
[37]X. He, M. Song, H. Liang, and C. Pan, J. Chem. Phys. **114**, 10510 (2001).
[38]Y. Wu, G. Cheng, K. Kastov, W. W. Sides, J. Wang, J. Tang, G. H. Fredrickson, M. Moskovits, and G. D. Stucky, Nature Mater. **3**, 816 (2004).
[39]H. Q. Xiang, K. Shin, T. Kim, S. I. Moon, T. J. McCarthy, and T. P. Russell, Macromolecules **37**, 5660 (2004).
[40]K. Shin, H. Q. Xiang, S. I. Moon, T. Kim, T. J. McCarthy, and T. P. Russell, Science **306**, 76 (2004).
[41]W. Li, R. A. Wickham, and R. A. Garbary, Macromolecules **39**, 806 (2006).
[42]W. Li and R. A. Wickham, Macromolecules **39**, 8492 (2006).
[43]B. Yu, P. Sun, P. Chen, Q. Jin, D. Ding, B. H. Li, and A. C. Shi, Phys. Rev. Lett. **96**, 138306 (2006).
[44]J. Feng and E. Ruchenstein, Macromolecules **39**, 4899 (2006).
[45]J. Feng, H. Liu, and Y. Hu, Macromol. Theory Simul. **15**, 674 (2006).
[46]P. Chen, H. Liang, and A. C. Shi, Macromolecules **40**, 7329 (2007).
[47]Y. S. Jung, M. Jung, and C. A. Ross, Nano Lett. **8**, 2975 (2008).
[48]G. J. A. Sevink and A. V. Zvelindovsky, J. Chem. Phys. **128**, 084901 (2008).
[49]Y. C. Xu, W. H. Li, F. Qiu, Y. Y. Yang, and A. C. Shi, J. Phys. Chem. B **113**, 11153 (2009).
[50]V. Kalra, J. H. Lee, J. H. Park, M. Marquez, and Y. L. Joo, Small **5**, 2323 (2009).
[51]M. Ma, E. L. Thomas *et al.*, Macromolecules **43**, 3061 (2010).
[52]B. Yu, B. H. Li, Q. H. Jin, D. T. Ding, and A. C. Shi, Macromolecules **40**, 9133 (2007).
[53]S. J. Joen, G. R. Yi, C. M. Koo, and S. M. Yang, Macromolecules **40**, 8430 (2007).
[54]M. Pinna, X. H. Guo, and A. V. Zvelindovsky, Polymer **49**, 2797 (2008).
[55]T. Higuchi, A. Tajima, K. Motoyoshi, H. Yabu, and M. Shimomura, Angew. Chem., Int. Ed. **47**, 8044 (2008).
[56]S. Li, P. Chen, L. Zhang, and H. Liang, Langmuir **27**, 5081 (2011).
[57]S. B. Darling, Prog. Polym. Sci. **32**, 1152 (2007).
[58]C. R. Stewart-Sloan and E. L. Thomas, Eur. Polym. J. **47**, 630 (2011).
[59]B. Yu, P. C. Sun, T. H. Chen, Q. H. Jin, D. T. Ding, B. H. Li, and A. C. Shi, J. Chem. Phys. **126**, 204903 (2007).
[60]M. W. Matsen and M. Schick, Phys. Rev. Lett. **72**, 2660 (1994).
[61]G. H. Fredrickson, *The Equilibrium Theory of Inhomogeneous Polymers* (Oxford University Press, Oxford, 2006).
[62]G. Tzeremes, K. Ø. Rasmussen, T. Lookman, and A. Saxena, Phys. Rev. E **65**, 041806 (2002).
[63]K. Ø. Rasmussen and G. J. Kalosakas, J. Polym. Sci., Part B: Polym. Phys. **40**, 1777 (2002).
[64]A. W. Bosse, C. J. Garcia-Cervera, and G. H. Fredrickson, Macromolecules **40**, 9570 (2007).
[65]Y. Oono and S. Puri, Phys. Rev. Lett. **58**, 836 (1987); Phys. Rev. A **38**, 434 (1988); **38**, 1542 (1988).
[66]I. W. Hamley, Macromol. Theory Simul. **9**, 363 (2000).
[67]I. W. Hamley, Angew. Chem., Int. Ed. **42**, 1692 (2003).
[68]A.-C. Shi, *Development in Block Copolymer Science and Technology*, edited by I. W. Hamley (Wiley, New York, 2004).
[69]D. Meng and Q. Wang, J. Chem. Phys. **126**, 234902 (2007).
[70]W. H. Li and R. A. Wickham, Macromolecules **42**, 7530 (2009).
[71]T. Ohta and K. Kawasaki, Macromolecules **19**, 2621 (1986).
[72]M. Nonomura and T. Ohta, J. Phys.: Condens. Matter **13**, 9089 (2001).
[73]C. K. Harrison *et al.*, Europhys. Lett. **67**, 800 (2004).
[74]D. A. Vega *et al.*, Phys. Rev. E **71**, 061803 (2005).